Towards carbon nanotube growth into superconducting microwave resonator geometries

S. Blien [1], K. J. G. Götz [1], P. L. Stiller [1], T. Mayer [1], T. Huber [1], O. Vavra [1], and A. K. Hüttel[*,1]

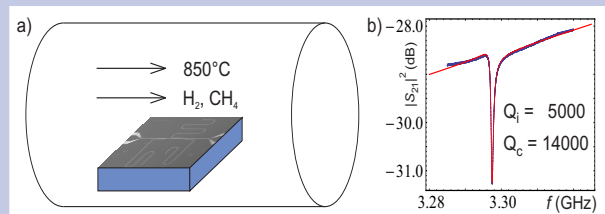[1] Institute for Experimental and Applied Physics, University of Regensburg, Universitätsstr. 31, 93053 Regensburg, Germany

[*] Corresponding author: e-mail andreas.huettel@ur.de, Phone: +49 941 943 1618, Fax: +49 941 943 3196

The in-place growth of suspended carbon nanotubes facilitates the observation of both unperturbed electronic transport spectra and high-Q vibrational modes. For complex structures integrating, e.g., superconducting rf elements on-chip, selection of a chemically and physically resistant material that survives the chemical vapor deposition (CVD) process provides a challenge.

We demonstrate the implementation of molybdenum-rhenium coplanar waveguide resonators that exhibit clear resonant behaviour at cryogenic temperatures even after having been exposed to nanotube growth conditions. The properties of the MoRe devices before and after CVD are compared to a reference niobium device.

(a) Schematic of the CVD growth environment; a metal thin film is exposed to a CH_4 / H_2 atmosphere at $850°C$. (b) MoRe coplanar waveguides still display superconductivity after this treatment, with clear resonant behaviour of a $\lambda/4$ structure.

1 Introduction The integration of different types of mesoscopic systems into hybrid device geometries has led to a multitude of experimental insights. One recent development is the application of coplanar waveguide resonator technology in hybrid quantum systems, see e.g. [1] for a detailed review of performed and possible experiments. Recently significant advances were made combining superconducting rf systems with with semiconductor quantum dots [2–4], and also in particular carbon nanotubes. Carbon nanotube quantum dots have been coupled into superconducting rf hybrid systems, targetting, e.g., non-equilibrium charge dynamics [5], noise spectroscopy [6, 7], and manipulation of spin states towards quantum information processing [8].

On their own, clean carbon nanotubes, as quasi-one dimensional carbon macromolecules, excel in their electronic [6,9–14] as well as nanomechanical properties [15–20]. This emerges in particular clearly if fabrication steps after nanotube growth, as, e.g., wet chemistry or lithography, are kept to a minimum. Several strategies to that ef-

fect are possible. A well established method is to grow the carbon nanotubes via chemical vapor deposition (CVD) in situ across pre-defined electrodes [9]. This generally leads to low contact resistance as well as devices resilient to mechanical vibrations or temperature changes. At the same time, the choice of materials is strongly restricted; contacts and other chip structures as, e.g., gates or isolation oxides, have to survive the CVD process, where the devices are exposed to hot and chemically aggressive gas mixtures. Metal thin films melt or deform strongly, or incorporate carbon or hydrogen. In particular, superconductors may display a strong decrease of their critical temperature. In addition the carbon nanotubes grow at random orientation and length, lowering the device yield.

This has recently led to the development of alternative strategies for the implementation of defect- and contamination-free suspended nanotube devices, and to first corresponding superconductor–nanotube hybrid experiments [6]. Typically the nanotubes are grown on a separate substrate and then transferred onto the readily

structured device at last instance [20–24, 6, 7]. The separation of growth and measurement onto different substrates allows a wider choice in device materials and targetted placement of the nanotubes, but may come at other costs. Surface oxidation or contamination of the metallic electrodes may require an additional annealing step to obtain transparent contacts; even cleaning the metal surfaces in situ using argon ion-etching and then keeping them in vacuum during transfer and measurement [23] has been performed. Conversely, the nanotube transfer process can be repeated while monitoring device performance, which for complex device geometries may lead to a higher yield of functioning structures [23, 6, 7].

Here, in preparation for the in-place growth approach, we use the CVD process environment to simulate nanotube growth across pre-defined electrodes and investigate metal films with/without having undergone CVD. For high-frequency experiments, where a suspended carbon nanotube is to be coupled to, e.g., a coplanar microwave resonator, a physically and chemically stable metal is required that remains superconducting even after incorporation of carbon and possible segregation processes during the high-temperature step. We characterize coplanar waveguide resonators fabricated from the co-sputtered molybdenum-rhenium alloy $Mo_{20}Re_{80}$ [25]. Even after CVD clear resonant behaviour is observed. We compare the device parameters with a reference niobium device and analyze the temperature dependence of resonance frequency and quality factor.

2 Carbon nanotube CVD growth process Our carbon nanotube growth via CVD follows a well-established process [26] that is able to produce few clean single-wall carbon nanotubes. The nanotubes grow from well-defined positions and subsequently fall over contact structures.

A catalyst suspension consisting of iron(III) nitrate nonahydrate $Fe(NO_3)_3 \cdot 9H_2O$, molybdenum dioxydiacetylacetonate $MoO_2(acac)_2$, and Al_2O_3 nanoparticles in methanol is used. The catalyst deposition area is defined lithographically. Following development of the electron-beam resist, the catalyst suspension is drop-cast onto the chip, and the solvent is evaporated on a hot plate at $150\,°C$. After a lift-off step, only the catalyst in the growth area remains on the chip. The devices are then placed into a $1''$ quartz tube, where they are heated up in an argon and hydrogen gas flow to a temperature of $850\,°C$. As soon as the temperature is reached, the argon flow is stopped and the devices are exposed to a hydrogen ($20\,sccm$) / methane ($10\,sccm$) atmosphere for ten minutes. During this time, the growth of the carbon nanotubes takes place. Afterwards, the devices are cooled down again under argon and hydrogen flow. Nanotube devices can now be electronically tested and pre-characterized.

For the thin-film material tests presented here, focussing on the effect of the high-temperature process on the metal films of the devices, both lithography and catalyst deposition steps are omitted for simplicity. The high-temperature process is performed in an identical way as actual nanotube CVD growth.

3 Resonator device fabrication and basic properties Two types of substrate form the starting point of device fabrication, either crystalline Al_2O_3 or compensation-doped Si with a $500\,nm$ thermally grown oxide. A metal layer is sputter-deposited and structured via optical lithography and reactive ion etching. Fig. 1(a) shows a resulting reference device, in this case made of niobium on a Si/SiO_2 substrate, containing three $\lambda/4$ resonators capacitively coupled to a common feed line. In Fig. 1(b), in a transmission measurement at $T = 4.2\,K$ the resonances of the $\lambda/4$ structures can be clearly identified as distinct minima of the feed line power transmission $|S_{21}|^2$.

The required resonator lengths for intended design frequencies can be calculated following

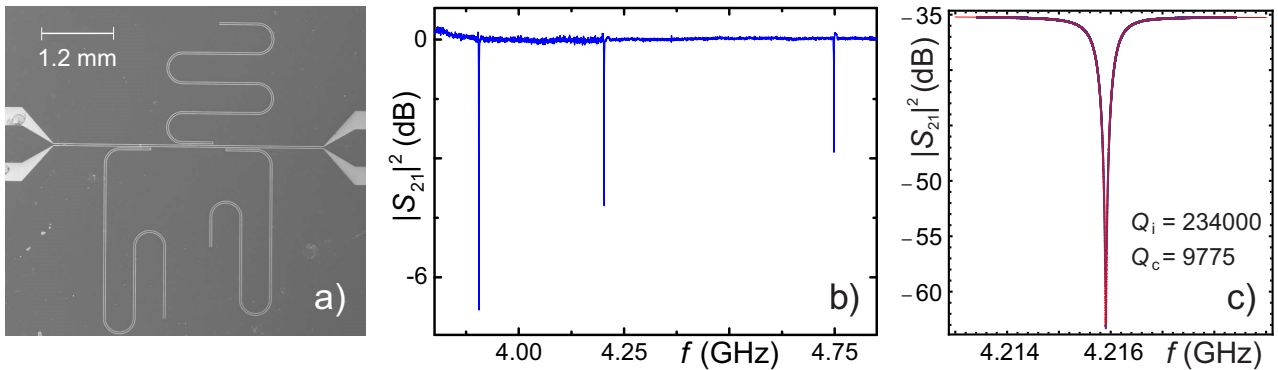$$f_r = \sqrt{\frac{1-\alpha}{\epsilon_{\text{eff}}}} \frac{c}{4l} \qquad (1)$$

where α is the kinetic inductance fraction of the superconductor, discussed below in more detail, l is the length of the resonator, and ϵ_{eff} is an effective relative permittivity resulting from the substrate below and the vacuum (or helium, depending on the measurement; both with $\epsilon_r \simeq 1$) above the substrate. In the simple case of a uniform substrate with permittivity ϵ_r, ϵ_{eff} can be approximated as $\epsilon_{\text{eff}} = (\epsilon_r + 1)/2$.

Fig. 1(c) displays a detail measurement of the reference device from (b) in a dilution refrigerator at $T = 15\,mK$. The overall transmission values are setup-specific, resulting from an attenuation of $-53\,dB$ for thermal coupling in the signal input line and an amplification of $+29\,dB$ via a HEMT amplifier [27] at the 1K stage in the signal output line. We experimentally determine a center frequency of $f_r \approx 4.2159\,GHz$.

Aside from the center frequency f_r, the resonance is characterized by the intrinsic quality factor Q_i, describing energy loss within the resonator, and the coupling quality factor Q_c, describing energy transfer from and to the feed line. The so-called loaded quality factor $Q_l = 1/\left(1/Q_i + 1/Q_c\right)$ combines both. The solid line in Fig. 1(c) is a fit following [28, 29], where the transmission (scattering matrix) parameter S_{21} is expressed as

$$S_{21} = 1 - \frac{\frac{Q_l}{|Q_e|}\, e^{i\theta}}{1 + 2iQ_l \frac{f-f_r}{f_r}}. \qquad (2)$$

Here, $Q_e = |Q_e| e^{-i\theta}$ has been additionally introduced, a complex-valued parameter related to the coupling quality factor Q_c as $Q_c^{-1} = \text{Re}\, Q_e^{-1}$, while $\text{Im}\, Q_e$ represents resonance asymmetries. For the reference device of Fig. 1(c) we find at $T = 15\,mK$ values of $Q_i = 234000$ and $Q_c = 9775$, demonstrating the quality of our niobium films

Figure 1 (Color online) (a) SEM image of a device containing three $\lambda/4$ superconducting coplanar waveguide resonators of different length, coupled to a common feed line, on a dielectric substrate. (b) Transmission spectrum ($T = 4.2\,\mathrm{K}$) of the feed line of a device with geometry as depicted in (a); 130nm niobium sputtered onto a silicon substrate with 500nm thermally grown SiO_2 cap layer. The spectrum is normalized to the high-power transmission where superconductivity within the resonators is suppressed. (c) Exemplary detail measurement of a resonance of the device from (b) at $T = 15\,\mathrm{mK}$; the solid red line is a fit (see text) resulting in $Q_i = 234000$ and $Q_c = 9775$.

and the lithographic patterning as well as the function of our measurement setup.

4 Molybdenum-rhenium as resonator material

While niobium is a well-established material for superconducting coplanar radiofrequency circuit elements, its thin films unfortunately do not survive the conditions of CVD carbon nanotube growth. Platinum cap layers on niobium have been used successfully in literature [30], but turned out to be unreliable in our testing. Rhenium thin films are stable under CVD conditions [12,18], however in our observation the critical temperature typically decreases below 1 K. A highly promising material is given by molybdenum-rhenium alloys. Pristine films have been shown to exhibit critical temperatures up to 15 K [31–33]. In addition, the films remain stable under CVD conditions [25,34,35]. While a significant amount of carbon is integrated into the metal, the high temperature process even leads to annealing-like processes and an initial increase in critical temperature, current and field [25,35,36].

Fig. 2(a) shows transmission resonances of three lithographically identical $\lambda/4$ structures, using different metallization layers. The rightmost resonance at highest frequency (black) uses niobium, the middle one (red) pristine molybdenum-rhenium, and the left one (blue) molybdenum-rhenium which has undergone the CVD process used for carbon nanotube growth. The molybdenum-rhenium 20:80 thin films have been deposited via simultaneous sputtering from two sources and their composition, identical for all devices discussed here, has been verified via x-ray photoelectron spectroscopy [25].

The difference in resonance frequency predominantly stems from a difference in the so-called kinetic inductance of the waveguide: the inertia-delayed response of charge carriers to a high-frequency field is mathematically equiv-

alent to an increased inductance and can be described as such. It leads to an additional contribution L_k to the inductance per length of the coplanar waveguide. Given the geometric, temperature-independent inductance per length L_g of a waveguide, the so-called kinetic inductance fraction is then defined as $\alpha = L_k/(L_g + L_k)$.
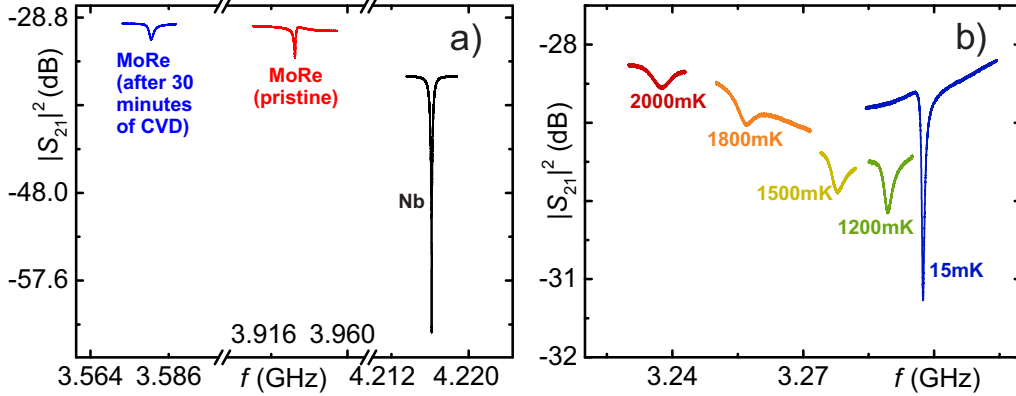
From the data of Fig. 2(a), assuming a small kinetic inductance fraction for niobium $\alpha_{\mathrm{Nb}} \simeq 0$ at dilution refrigerator base temperature $T = 15\,\mathrm{mK}$, we obtain using Eq. 1 from the resonance frequency for the molybdenum-rhenium device before CVD $\alpha_{\mathrm{MoRe}} = 1-(f_0^{\mathrm{MoRe}}/f_0^{\mathrm{Nb}})^2 = 0.131$ and after CVD $\alpha_{\mathrm{MoRe,CVD}} = 0.279$.

Via fitting to Eq. 2 we obtain the quality factors Q_i and Q_c of the resonator structures. The coupling quality factor Q_c is similar ($Q_c \sim 10^4$) for all three devices, consistent with the identical geometry and thereby coupling capacitance. For the intrinsic quality factor we here obtain $Q_i = 234000$ for Nb, $Q_i = 20800$ for MoRe without CVD exposure, and $Q_i = 2700$ for MoRe after 30min CVD exposure. Q_i differs strongly, due to the presence of quasiparticle excitations and corresponding dissipation (see following section).

5 Temperature dependence of resonator properties

Fig. 2(b) shows the resonance of the CVD-treated molybdenum-rhenium device from Fig. 2(a), at differing temperature. The resonance frequency f_r decreases strongly with temperature, as does the total quality factor. A quantitative description of this is given by the so-called Mattis-Bardeen theory [25,37]. The temperature dependence of f_r and Q_i can be expressed as

$$\frac{f_r - f_0}{f_0} = \frac{\alpha_0}{2}\frac{\delta\sigma_2}{\sigma_2}, \tag{3}$$
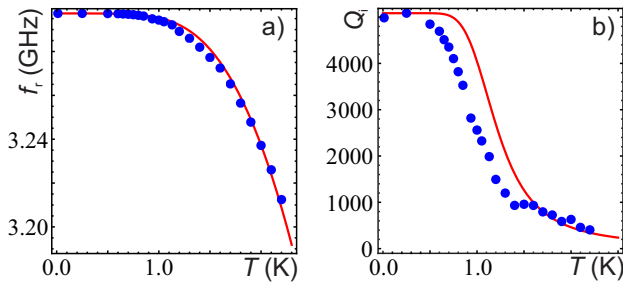
Figure 2 (Color online) (a) Power transmission resonances $|S_{21}|^2 (f)$ at $T = 15$ mK of three lithographically identical $\lambda/4$ structures (see Fig. 1(a) for the optical mask geometry). The patterned thin film consists of 130nm Nb (right resonance), 145nm pristine $Mo_{20}Re_{80}$ (middle resonance), and 145nm $Mo_{20}Re_{80}$ after undergoing 30 min of CVD process (left resonance). The distinct shift in the resonance frequency f_r is caused by different kinetic inductance fractions α for the different materials. (b) $|S_{21}|^2 (f)$ at the resonance of the CVD-treated $Mo_{20}Re_{80}$ device from (a), for temperatures 15 mK $\leq T \leq 2$ K.

$$\delta \left(\frac{1}{Q_i} \right) = \alpha_0 \frac{\delta \sigma_1}{\sigma_2}, \tag{4}$$

with f_0 and α_0 as the zero-temperature limit of resonance frequency and kinetic inductance fraction. σ_1 and σ_2 are the real and imaginary part of the complex conductivity σ of the device. We use analytical approximations for both parts of the complex conductivity in the low temperature limit [25,38], containing the temperature dependent BCS energy gap and the normal state conductivity.

Figure 3 shows the extracted resonance frequency f_r

Figure 3 (a) Resonance frequency $f_r(T)$ and (b) internal quality factor $Q_i(T)$ as function of temperature, for the device of Fig. 2(b) (145 nm MoRe, after 30 min CVD conditions). The red lines show fit curves using Mattis-Bardeen-theory, see the main text.

(Fig. 3(a)) and internal quality factor Q_i (Fig. 3(b)) as function of temperature T. The solid line in Fig. 3(a) is a fit following Eq. 3, with α_0 as the only free fit parameter. Using a critical temperature of $T_c = 4$ K determined via dc measurements, the fit results in $\alpha_0 = 0.361$. This is larger than the value we found by comparing the resonance fre-
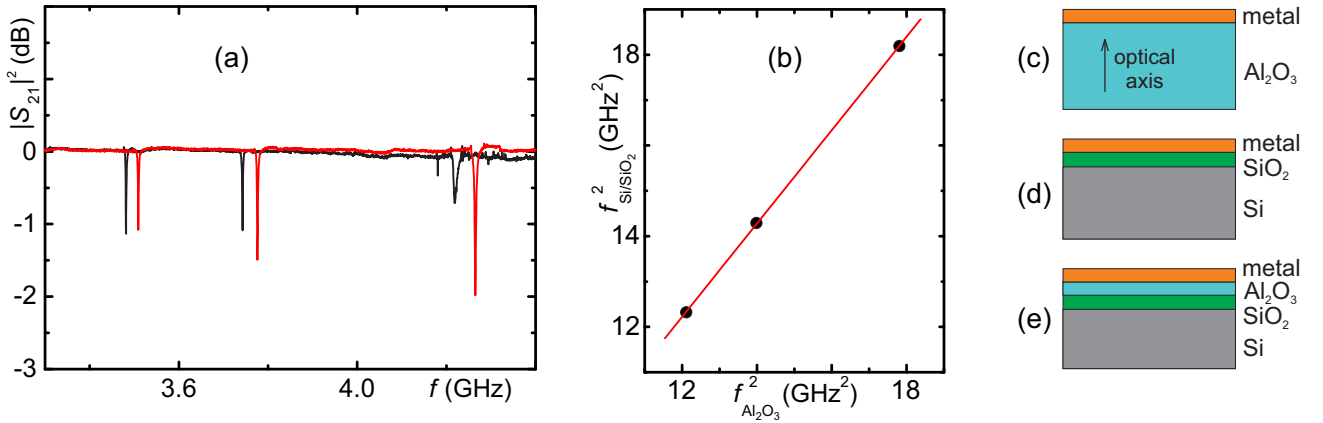
quencies of different materials in Sec. 4, however, a smooth drop of the resistance in dc measurements makes a precise determination of T_c difficult.

In the same manner, we obtain $\alpha_0 = 0.176$ for the pristine MoRe device, and $\alpha_0 = 0.029$ for the niobium device. The value of α_0 for the MoRe device is comparable to the one of Sec. 4, while the value for the niobium device confirms that $\alpha \approx 0$ was a good approximation. Generally, we find small kinetic inductance fractions for niobium and intermediate ones for MoRe, with increasing values for increasing CVD exposure time, corresponding to deterioration of the superconducting properties.

Regarding the intrinsic quality factor Q_i in Fig. 3(b), we use the value $\alpha_0 = 0.361$ extracted from the fit of Fig. 3(a), and plot the theoretical result following Eq. 4 without additional free parameters. The result (solid red line) displays acceptable agreement with the data points. However, models more complex than the straightforward Mattis-Bardeen description may be appropriate, see, e.g., [39] for the integration of a finite quasiparticle lifetime.

6 Impact of the substrate material Two different substrate materials have been tested, on one hand crystalline Al_2O_3 (Fig. 4(c)), on the other highly resistive silicon with a thermally (dry) grown, 500nm thick SiO_2 cap layer (Fig. 4(d)). The dielectric constant of the substrate ϵ_r enters the resonance frequency via Eq. 1. Fig. 4(a) displays the transmission spectrum of two devices using the same lithographic structure and metal film (pristine MoRe), but different substrates.

As a consistency check, we can compare the resonance positions, deduce the effective permittivity of the Si/SiO_2 bilayer, and compare it with a calculation. Using Eq. 1 it

Figure 4 (a) Transmitted signal $|S_{21}|^2$ for two devices made of molybdenum-rhenium using the same optical mask, but different substrate materials. The shift in resonance frequency is caused by different relative permittivities of the substrates (red: Si/SiO$_2$, black: Al$_2$O$_3$). (b) The ratio of the squared resonance frequencies is used to determine the relative permittivity of Si/SiO$_2$. (c) - (e) Different substrate structures: (c) crystalline Al$_2$O$_3$, (d) compensation-doped silicon with 500nm of SiO$_2$ on top, (e) same as in (d) with an additional layer of Al$_2$O$_3$ that was grown using atomic layer deposition.

is easy to show that the effective dielectric constants of the two devices relate to the resonance frequencies as

$$\frac{\epsilon_{\text{eff}}^{\text{Al}_2\text{O}_3}}{\epsilon_{\text{eff}}^{\text{Si/SiO}_2}} = \left(\frac{f_{\text{r}}^{\text{Si/SiO}_2}}{f_{\text{r}}^{\text{Al}_2\text{O}_3}} \right)^2, \qquad (5)$$

with $\epsilon_{r,\perp}^{\text{Al}_2\text{O}_3} = 9$ and $\epsilon_{\text{eff}}^{\text{Al}_2\text{O}_3} = 5$. From the data of Fig. 4(a,b) we obtain $\epsilon_{\text{eff}}^{\text{Si/SiO}_2} = 4.86$. Using the geometrical device dimensions and following [40] leads to an expected value of $\epsilon_{\text{eff}} = 4.88$ and thereby to excellent agreement with the experimentally determined value.

For integrating carbon nanotube quantum dot structures with coplanar resonators, additional gate isolation layers are desirable. With this in mind we have tested additionally inserted oxide layers below the superconducting coplanar waveguide. This is sketched in Fig. 4(e), where an additional Al$_2$O$_3$ layer has been grown using atomic layer deposition before applying the resonator metallization. In a final device this layer could, e.g., separate contact electrodes and nanotube from local top gate electrodes.

Table 1 shows an overview of internal quality factors Q_{i} at $T = 4.2\,\text{K}$ of devices without or with additional Al$_2$O$_3$ layer below pristine molybdenum-rhenium. While there is a certain scatter, no clear tendency towards lower or higher quality factor is recognizable; within the experimental resolution achievable at this temperature no impact of the layer can be seen.

7 Conclusion We demonstrate that $\lambda/4$ coplanar waveguide resonators fabricated from a molybdenum-rhenium alloy display resonant behaviour at millikelvin temperatures even after being exposed to the chemical vapor deposition conditions required for carbon nan-

Al$_2$O$_3$ thickness	f_{r} (GHz)	Q_{i} (4.2 K)
0 nm	3.510	2060
0 nm	3.777	2170
0 nm	4.265	1600
10 nm	3.560	2690
10 nm	3.840	2480
150 nm	3.576	2570
150 nm	3.842	1420
150 nm	4.350	1900

Table 1 Internal quality factors Q_{i} at $T = 4.2\,\text{K}$ of devices without or with additional Al$_2$O$_3$ layer below pristine molybdenum-rhenium, cf. Fig. 4(e). At this temperature within experimental scatter no impact of the Al$_2$O$_3$ on the quality factor can be seen.

otube growth. Compared to a reference niobium device, the resonance frequency of lithographically identical molybdenum-rhenium devices is lower due to a larger kinetic inductance fraction of the material. The temperature dependence of resonance frequency and internal quality factor can be well described by Mattis-Bardeen theory in the analyzed temperature range. Both Si/SiO$_2$ and Al$_2$O$_3$ substrates can be used, with the expected impact of the permittivities on the resonance frequency. An additional Al$_2$O$_3$ layer deposited on a Si/SiO$_2$ substrate via atomic layer deposition, which could, e.g., be used for nanotube top gate isolation, does not lead to any change in quality factor detectable at $T = 4.2\,\text{K}$.

While our thin film deposition via co-sputtering from two sources has the advantage of adjustable alloy composition [25], other published results using pre-alloyed sput-

ter targets display significantly higher quality factors [35]. Given our excellent results using niobium, we can exclude problems with substrate, lithography, and detection circuitry. Further work shall thus target additional optimization of the metal thin films regarding both nominal composition and detailed deposition parameters.

References

[1] Z. L. Xiang, S. Ashhab, J. Q. You, and F. Nori, Rev. Mod. Phys. **85**, 623–653 (2013).

[2] T. Frey, P. J. Leek, M. Beck, A. Blais, T. Ihn, K. Ensslin, and A. Wallraff, Phys. Rev. Lett. **108**, 046807 (2012).

[3] J. Basset, D. D. Jarausch, A. Stockklauser, T. Frey, C. Reichl, W. Wegscheider, T. M. Ihn, K. Ensslin, and A. Wallraff, Phys. Rev. B **88**, 125312 (2013).

[4] K. D. Petersson, L. W. McFaul, M. D. Schroer, M. Jung, J. M. Taylor, A. A. Houck, and J. R. Petta, Nature **490**, 380 (2012).

[5] J. J. Viennot, M. R. Delbecq, M. C. Dartiailh, A. Cottet, and T. Kontos, Phys. Rev. B **89**, 165404 (2014).

[6] V. Ranjan, G. Puebla-Hellmann, M. Jung, T. Hasler, A. Nunnenkamp, M. Muoth, C. Hierold, A. Wallraff, and C. Schönenberger, Nature Communications **6**, 7165 (2015).

[7] T. Hasler, M. Jung, V. Ranjan, G. Puebla-Hellmann, A. Wallraff, and C. Schönenberger, Phys. Rev. Applied **4**(Nov), 054002 (2015).

[8] J. J. Viennot, M. C. Dartiailh, A. Cottet, and T. Kontos, Science **349**(6246), 408–411 (2015).

[9] J. Cao, Q. Wang, and H. Dai, Nature Materials **4**(10), 745–749 (2005).

[10] F. Kuemmeth, S. Ilani, D. C. Ralph, and P. L. McEuen, Nature **452**(7186), 448–452 (2008).

[11] G. A. Steele, G. Götz, and L. P. Kouwenhoven, Nature Nanotechnology **4**(6), 363–367 (2009).

[12] D. R. Schmid, S. Smirnov, M. Margańska, A. Dirnaichner, P. L. Stiller, M. Grifoni, A. K. Hüttel, and C. Strunk, Physical Review B **91**, 155435 (2015).

[13] E. A. Laird, F. Kuemmeth, G. A. Steele, K. Grove-Rasmussen, J. Nygård, K. Flensberg, and L. P. Kouwenhoven, Rev. Mod. Phys. **87**, 703–764 (2015).

[14] A. Dirnaichner, M. del Valle, K. J. G. Götz, F. J. Schupp, N. Paradiso, M. Grifoni, A. K. Hüttel, and C. Strunk, submitted for publication (2016), arXiv:1602.03866.

[15] A. K. Hüttel, G. A. Steele, B. Witkamp, M. Poot, L. P. Kouwenhoven, and H. S. J. van der Zant, Nano Letters **9**(7), 2547–2552 (2009).

[16] J. Moser, A. Eichler, J. Güttinger, M. I. Dykman, and A. Bachtold, Nature Nanotechnology **9**(12), 1007–1011 (2014).

[17] G. A. Steele, A. K. Hüttel, B. Witkamp, M. Poot, H. B. Meerwaldt, L. P. Kouwenhoven, and H. S. J. van der Zant, Science **325**(5944), 1103–1107 (2009).

[18] D. R. Schmid, P. L. Stiller, C. Strunk, and A. K. Hüttel, New Journal of Physics **14**(8), 083024 (2012).

[19] D. R. Schmid, P. L. Stiller, C. Strunk, and A. K. Hüttel, Appl. Phys. Lett. **107**(12), 123110 (2015).

[20] A. Benyamini, A. Hamo, S. V. Kusminskiy, F. von Oppen, and S. Ilani, Nature **10**, 151–156 (2014).

[21] C. C. Wu, C. H. Liu, and Z. Zhong, Nano Letters **10**(3), 1032–1036 (2010).

[22] F. Pei, E. A. Laird, G. A. Steele, and L. P. Kouwenhoven, Nature Nanotechnology **7**(10), 630–634 (2012).

[23] J. Waissman, M. Honig, S. Pecker, A. Benyamini, A. Hamo, and S. Ilani, Nature Nanotechnology **8**, 569–574 (2013).

[24] J. Gramich, A. Baumgartner, M. Muoth, C. Hierold, and C. Schönenberger, physica status solidi (b) **252**(11), 2496–2502 (2015).

[25] K. J. G. Götz, S. Blien, P. L. Stiller, O. Vavra, T. Mayer, T. Huber, T. N. G. Meier, M. Kronseder, C. Strunk, and A. K. Hüttel, Nanotechnology **27**, 135202 (2016).

[26] J. Kong, H. T. Soh, A. M. Cassell, C. F. Quate, and H. Dai, Nature **395**(6705), 878 (1998).

[27] Caltech CITCRYO1-12A cryogenic microwave amplifier, http://www.caltechmicrowave.org/.

[28] M. S. Khalil, M. J. A. Stoutimore, F. C. Wellstood, and K. D. Osborn, Journal of Applied Physics **111**(5), 054510 (2012).

[29] A. Bruno, G. de Lange, S. Asaad, K. L. van der Enden, N. K. Langford, and L. DiCarlo, Appl. Phys. Lett. **106**(18), 182601 (2015).

[30] M. R. Delbecq, V. Schmitt, F. D. Parmentier, N. Roch, J. J. Viennot, G. Fève, B. Huard, C. Mora, A. Cottet, and T. Kontos, Phys. Rev. Lett. **107**(Dec), 256804 (2011).

[31] L. R. Testardi, J. J. Hauser, and M. H. Read, Solid State Communications **9**, 1829–1831 (1971).

[32] J. R. Gavaler, M. A. Janocko, and C. K. Jones, Applied Physics Letters **21**(4), 179–180 (1972).

[33] V. S. Postnikov, V. V. Postnikov, and V. S. Zheleznyi, Physica Status Solidi A **39**, 21–23 (1977).

[34] B. H. Schneider, S. Etaki, H. S. J. van der Zant, and G. A. Steele, Scientific Reports **2**, 599 (2012).

[35] V. Singh, B. H. Schneider, S. J. Bosman, E. P. J. Merkx, and G. A. Steele, Applied Physics Letters **105**, 222601 (2014).

[36] M. Aziz, D. C. Hudson, and S. Russo, Applied Physics Letters **104**, 233102 (2014).

[37] D. C. Mattis and J. Bardeen, Phys. Rev. **111**, 412–417 (1958).

[38] J. Gao, J. Zmuidzinas, A. Vayonakis, P. Day, B. Mazin, and H. Leduc, Journal of Low Temperature Physics **151**, 557–563 (2008).

[39] M. Žemlička, P. Neilinger, M. Trgala, M. Rehák, D. Manca, M. Grajcar, P. Szabó, P. Samuely, i. c. v. Gaži, U. Hübner, V. M. Vinokur, and E. Il'ichev, Phys. Rev. B **92**, 224506 (2015).

[40] E. Chen and S. Y. Chou, IEEE Transactions on Microwave Theory and Techniques **45**, 939–945 (1997).